Staufer, O., Antona, S., Zhang, D., Csatári, J., Schröter, M., Janiesch, J-W., Fabritz, S., Berger, I., Platzman, I., & Spatz, J. P. (2021). Microfluidic production and characterization of biofunctionalized giant unilamellar vesicles for targeted intracellular cargo delivery. *Biomaterials*, *264*, [120203]. https://doi.org/10.1016/j.biomaterials.2020.120203

Biomaterials 264 (2021) 120203

Contents lists available at ScienceDirect

Biomaterials

journal homepage: www.elsevier.com/locate/biomaterials

Microfluidic production and characterization of biofunctionalized giant unilamellar vesicles for targeted intracellular cargo delivery

Oskar Staufer[a,b,c,*], Silvia Antona[a,b], Dennis Zhang[a], Júlia Csatári[a], Martin Schröter[a,b], Jan-Willi Janiesch[a,b], Sebastian Fabritz[d], Imre Berger[c,e,f], Ilia Platzman[a,b,c,**], Joachim P. Spatz[a,b,c,***]

[a] Department for Cellular Biophysics, Max Planck Institute for Medical Research, Jahnstraße 29, 69120 Heidelberg, Germany
[b] Institute for Molecular Systems Engineering (IMSE), Heidelberg University, D-69120 Heidelberg, Germany
[c] Max Planck-Bristol Center for Minimal Biology, University of Bristol, 1 Tankard's Close, Bristol BS8 1TD, UK
[d] Department for Chemical Biology, Max Planck Institute for Medical Research, Jahnstraße 29, 69120, Heidelberg, Germany
[e] School of Biochemistry, Biomedical Sciences, University of Bristol, 1 Tankard's Close, Bristol BS8 1TD, UK
[f] Bristol Synthetic Biology Centre BrisSynBio, University of Bristol, 4 Tyndall Ave, Bristol BS8 1TQ, UK

ARTICLE INFO

Keywords:
Giant unilamellar vesicles
Targeted delivery
GUV-cell interactions
Microfluidics

ABSTRACT

Lipid-based vesicles have found widespread applications in the life sciences, allowing for fundamental insights into membrane-based processes in cell biology and as carrier systems for drug delivery purposes. So far, mostly small unilamellar vesicles (SUVs) with diameters of ~100 nm have been applied as carrier systems for biomedical applications. Despite this progress, several systematic limitations have arisen due to SUV dimensions, *e.g.,* the size and total amount of applicable cargo is limited. Giant unilamellar vesicles (GUVs) might offer a pragmatic alternative for efficient cargo delivery. However, due to the lack of reliable high-throughput production technologies for GUV-carrier systems, only little is known about their interaction with cells. Here we present a microfluidic-based mechanical droplet-splitting pipeline for the production of carrier-GUVs with diameters of ~2 μm. The technology developed allows for highly efficient cargo loading and unprecedented control over the biological and physicochemical properties of GUV membranes. By generating differently charged (between −31 and + 28 mV), bioligand-conjugated (e.g. with E-cadherin, NrCam and antibodies) and PEG-conjugated GUVs, we performed a detailed investigation of attractive and repulsive GUV-cell interactions. Fine-tuning of these interactions allowed for targeted cellular GUV delivery. Moreover, we evaluated strategies for intracellular GUV cargo release by lysosomal escape mediated by the pH sensitive lipid DOBAQ, enabling cytoplasmic transmission. The presented GUV delivery technology and the systematic characterization of associated GUV-cell interactions could provide a means for more efficient drug administration and will pave the way for hitherto impossible approaches towards a targeted delivery of advanced cargo such as microparticles, viruses or macromolecular DNA-robots.

1. Introduction

Lipid-based SUVs, with diameters ~100 nm, have been extensively studied as transport systems in the food, cosmetic and pharmaceutical industries. Particularly, they have been implemented to serve as nanosensors for monitoring food quality during storage [1], as vehicles for the transdermal delivery of cosmetic agents [2], or as carrier systems for targeted drug therapy [3]. Such liposomal delivery systems offer improved control over drug pharmacokinetics and pharmacodynamics [4], provide the potential to decrease toxicity and adverse side effects [5], enhance targeted delivery to specific tissues [6] and increase compound circulation times [5].

Despite the beneficial impact of SUV-based delivery systems, the road towards their broad applicability remains complex. The major challenges that are currently faced fall into two broad categories. First, the total amount of pharmaceutically active compounds that can be entrapped in a single liposome is meager, potentially not reaching the desired therapeutic dose at its destination [7]. Second, entrapment efficiency into liposomes is usually very low (around 10% for water-soluble compounds) and active loading approaches are complex, expensive and time

* Corresponding authors. Department for Cellular Biophysics, Max Planck Institute for Medical Research, Jahnstraße 29, 69120, Heidelberg, Germany
** Corresponding authors. Department for Cellular Biophysics, Max Planck Institute for Medical Research, Jahnstraße 29, 69120, Heidelberg, Germany
*** Corresponding authors. Department for Cellular Biophysics, Max Planck Institute for Medical Research, Jahnstraße 29, 69120 Heidelberg, Germany
E-mail addresses: oskar.staufer@mr.mpg.de (O. Staufer), ilia.platzman@mr.mpg.de (I. Platzman), joachim.spatz@mr.mpg.de (J.P. Spatz).

https://doi.org/10.1016/j.biomaterials.2020.120203
Received 23 October 2019; Received in revised form 27 May 2020; Accepted 9 June 2020
Available online 09 September 2020

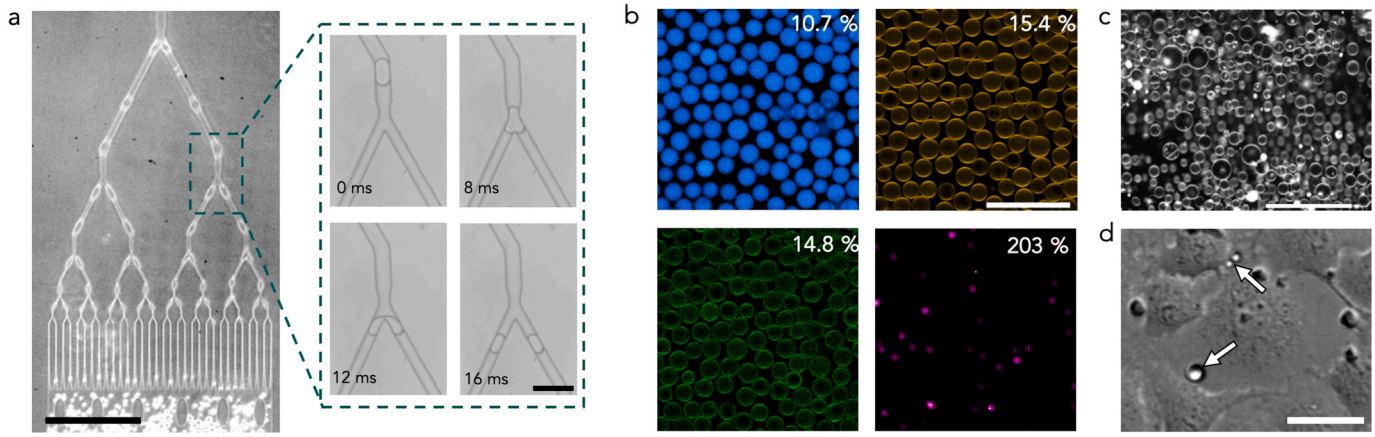

Fig. 1. Microfluidic formation of GUVs and their interactions with living cells. (a) Phase-contrast microscopy image showing the microfluidic device used for serial five-fold mechanical dsGUV division, resulting in the formation of 32 daughter droplets from a single 60 μm droplet. The inset shows a higher magnification of the mechanical division of a droplet at a V-junction over a time course of 16 msec. The scale bars are 300 μm (left) and 60 μm (right). (**b**) Single plane fluorescence confocal microscopy images of mechanically split droplets loaded with AlexaFluor 405 (blue), fluorescently labeled SUVs (1 mol% LissRhod PE, yellow), green fluorescent protein (green) and 1 μm fluorescent polystyrene beads (purple). Upper right corner indicates CV of the droplet mean signal intensity (n = 665 single droplets). The scale bar is 40 μm. (**c**) Single plane fluorescence confocal microscopy images of split GUVs (20 mol% EggPG, 79 mol% EggPC and 1 mol% LissRhod PE) released in PBS. The scale bar is 25 μm. (**d**) Representative phase contrast image of mechanically split GUVs incubated with rat embryonic fibroblasts. White arrows indicate single GUVs. The scale bar is 10 μm. See Table S1 for details on the lipid and buffer compositions.

consuming [8,9]. Moreover, large cargos are expected to be part of future therapeutic approaches, including nanoparticles or supramolecular DNA and RNA complexes. For instance, DNA origami complexes have been proposed to enhance chemotherapies and fluorescent semiconductor nanocrystals (nano dots) have proven to improve *in vivo* imaging approaches [10,11]. Loading such large cargo into small liposomes is extremely challenging if not impossible. GUVs, in contrast, with radii exceeding 1 μm might thus offer great potential for drug delivery applications, as they can carry much larger quantities of active compounds as well as particles up to several micrometers in size [12,13].

With the recent rise of bottom-up synthetic biology, GUVs have seen a science community-wide surge in popularity for other uses as well. In this context, GUV-based compartments have been designed to recreate the essential characteristics of life as described by the Chemoton model [14]. This gave rise to several microfluidic GUV production techniques like double emulsion methods [15], octanol assisted liposome assembly [16], microfluidic multicompartment synthetic cells [17] and multi-module devices for microfluidic handling of GUVs [18]. Research in this area is currently focused on the construction of synthetic cellular constituents and artificial cells which serve as biomimetic systems that incorporate cell-like structures and exhibit cell-like behavior [19]. In addition to the attention on fully synthetic cell systems, a special focus has also been laid on hybrid systems, which are used to investigate interactions between synthetic cell-like GUVs with living cells [20].

Despite the growing demand for GUV-based biomedical and synthetic biology applications, the potential of GUVs to deliver large and complex cargos into the intracellular space or, in general, their ability to interact with living cells have been only superficially explored to date [21]. In this study, we characterized physical, chemical and biological key parameters that conquer the interactions between living cells and GUVs. Towards this end, we implemented the recently developed droplet-based microfluidic method for high-throughput production of large, surfactant-free GUV quantities with exquisite entrapment efficiencies of small molecules and micrometer-sized particles [22,23,54]. This production method for droplet-stabilized GUVs (dsGUVs) offers a high level of control over lipid and luminal composition (see Supplementary Note 1) as well as a large spectrum of compatible buffer compositions, rendering it an attractive technology for the controlled synthesis of GUVs with tunable properties for drug delivery and synthetic biology studies [19,24]. Using this technology, we here provide a first comprehensive and thorough analysis of GUV-cell interactions and present a concept for targeted GUV-mediated delivery into cells.

2. Results and discussion

2.1. Microfluidic mechanical splitting of droplet-stabilized GUVs

Assembling GUVs from SUV precursors within microfluidic water-in-oil (w/o) droplet architectures offers excellent control over GUV composition as well as high production rates [23]. This approach has previously been used to produce cell-sized or even larger GUVs with diameters of ~50 μm, which have served as durable, excellent to handle and low-cost mimics of living cells as their unilamellar membrane closely resembles a cellular membrane [22–24]. However, GUVs identical or larger in size than typical cells are of limited use for intracellular delivery strategies (see Figure S1). Downsizing droplets to produce GUV sizes smaller than 5 μm using flow focusing junctions requires sophisticated lithography procedures and complex channel architectures, measures that restrict reliable high-throughput small-droplet production [25,26]. To overcome these technological limitations, we designed a droplet-based microfluidic device consisting of a flow focusing junction for w/o-droplet production and a multi-V-shaped microfluidic droplet splitting unit (Fig. 1a, Figure S2). Similar microfluidic designs have previously been described for high throughput droplet-splitting [27,28]. Following production of 60 μm diameter droplets (See Experimental Section), this design allows for high-throughput mechanical droplet splitting in up to five consecutive division steps, thereby creating droplets with a final diameter of 2.90 μm ± 0.45 μm (n = 202) (Video S1).

Supplementary data related to this article can be found at https://doi.org/10.1016/j.biomaterials.2020.120203.

To assess transmission heterogeneity of intraluminal contents from the mother to the daughter droplets, we performed fluorescence confocal microscopy analysis of fluorescent droplet content and analyzed respective signal intensity distributions among droplets before and after splitting (Fig. 1b). The results revealed only marginal interdroplet variation of signal intensity for the low molecular weight fluorophore AlexaFluor 405 before splitting (Coefficient of variation (CV) $_{\text{before}}$ = 5.6%, n = 29) and after splitting (CV_{after} = 10.7%, n = 665), green fluorescent protein (CV_{before} = 18.5%, n = 29 and CV_{after} = 14.8%, n = 665) and 100 nm fluorescently labeled SUVs composed of 20 mol% EggPG, 79 mol% EggPC and 1 mol% LissRhod PE

(CV_{before} = 68.0%, n = 29 and CV_{after} = 15.4%, n = 665). Only 1 μm polystyrene beads showed asymmetric distribution after mechanical division, presumably because their size and concentration only allows for Bernoulli-like splitting distributions. Based on this, we concluded that the luminal composition of split droplets mostly resembles the composition of the mother droplets. Thus, our mechanical splitting approach is suitable for the controlled production of small w/o-droplets with defined and tunable compositions at high production rates (*e.g.,* 2.5×10^5 and 8×10^6 droplets/min at the focusing T-junction and after serially splitting the droplet five times, respectively). Importantly, we found peripheral distribution of lipid fluorescence in the divided droplets, suggesting the successful mechanical division of dsGUVs. Indeed, following the addition of destabilizing surfactant to the dsGUVs collected from mechanically split droplets (see Experimental Section), we were able to release large quantities of GUVs (diameter = 1.400 μm ± 0.202 μm, n = 122) into an aqueous phase (Fig. 1c). Note, 1.5 mM was found to be the optimal SUV concentration, achieving over 50% GUV release efficiency, corresponding to a successful release from approximately every second droplet (Fig. S3a). Under optimized conditions this method allows for a GUV production rate of approximately 4×10^6 GUVs/min.

Full control over the physicochemical and biological properties of GUVs is a pivotal requirement for biomedical and synthetic biology applications. Therefore, we applied mass spectrometry (see Experimental Section) to quantitatively assess the lipid composition of the formed GUVs. The results revealed that the GUV lipid ratio resembles the lipid ratio used during dsGUV production, thus indicating that the lipid ratio is unaffected by microfluidic handling and mechanical droplet splitting (Fig. S3b). Additionally, we performed a basic assessment of the mechanical stability of the formed GUVs and found that approximately 90% of the GUVs tolerate incubation at 37 °C and mechanical agitation on a horizontal shaker at 800 rpm for 24 h. This shows that released droplet-splitted GUVs are stable under agitation in a time frame required for most liposomal drug delivery applications [29] (Fig. S3c).

To successfully interface GUVs with living cells, it is critical to produce and maintain GUVs under physiological buffer conditions. Therefore, we systematically assessed the release efficiency of mechanically split GUVs filled with serum-supplemented cell culture medium. Similarly, to production with PBS and water, we obtained up to 45% release efficiency in cell culture medium (Fig. S3d). Following release, GUVs were incubated with rat embryonic fibroblasts (REF) in cell culture. Importantly, time-lapse microscopy analysis showed that these GUVs remained stable over a period of at least 20 h incubation (Fig. 1d and Video S2).

Supplementary data related to this article can be found at https://doi.org/10.1016/j.biomaterials.2020.120203.

2.2. Charge-mediated GUV- cell interactions

Charge-mediated interactions between liposomes and cells have been extensively studied for small vesicles (< 100 nm). These studies have pinpointed major factors that conquer the cell-vesicle interplay. Potentially, if precisely controlled, charge-mediated interactions might serve as a potent instrument to also guide the interactions between cells and GUVs. Therefore, we systematically investigated the interaction spectrum of differently charged mechanically split GUVs incubated with various cell lines *in vitro*. To this end, we employed mechanical splitting to produce GUVs with varying amounts of positively (DOTAP) and negatively (DOPG) charged lipids and measured their respective ζ-potential using dynamic light scattering (Table 1). We found that by altering the respective lipid amounts, the charge of the GUVs can be adjusted ranging from highly positive to highly negative charged vesicles.

To quantify the interactions between cells and GUVs, we implemented a plate reader-based attraction assay (Fig. S4) and interfaced cell lines of endothelial (MDCK), epithelial (A431D and A431) and adrenal (PC12) origin with respective GUVs. These cell lines were selected in order to cover a wide spectrum of possible target tissues with different surface patterns. We found a strong correlation between GUV charge and cell attraction for all tested cell lines, showing that any increase in charge results in a greater GUV attraction; non-charged GUVs displayed the least cell attraction (Fig. 2a). For example, in the case of A431D cells, a frequently used model cell line in carcinoma research, GUVs with a ζ-potential of −31 mV showed almost 100 times stronger attraction than GUVs with +2 mV ζ-potential. Inversely, GUVs with a ζ-potential of +28 mV had 50 times greater attraction than GUVs with +2 mV ζ-potential. However, this quantitative assay is not able to discriminate between different types of interactions (e.g., uptake, attachment, fusion or engulfment). Therefore, we investigated the qualitative nature of the GUV-cell interactions with fluorescence confocal microscopy. As shown in Fig. 2b, we were able to discriminate between three distinct types of GUV-A431D cell interactions: endocytosis, attachment and fusion. We also found the different types of cell interactions to be distinctly associated with specific states of charge – endocytosis is primarily observed on negatively charged GUVs, attachment with neutral GUVs and fusion with positively charges GUVs. Fusion was evident when lipid fluorescence co-localized with cell membrane staining (in many cases accompanied by morbid cell morphologies). To confirm that negatively charged GUVs are indeed taken up by the cells, we performed two additional analyses: First, we stained the cell's cytoplasm and performed z-resolved confocal fluorescence microscopy of internalized fluorescently labeled GUVs (Video S3). Second, we fixed the cells that have been incubated with respective GUVs and performed transmission electron microscopy (Fig. S4). Both assessments unequivocally proved that GUVs are indeed taken up by the cells and reside within their cytoplasm. Taken together, these results reveal the pervasive effects of GUV charge on GUV-cell interactions and highlight the value of developing methods for GUV charge control.

Table 1
ζ-potential values of the released GUVs that contained different lipid compositions and were created by microfluidic mechanical splitting of dsGUVs.

Lipid Type	Lipid ratio				
DOTAB (mol%)	0	0	0	20	50
DOPC (mol%)	49	79	99	79	49
DOPG (mol%)	50	20	0	0	0
LissRhod PE (mol%)	1	1	1	1	1
ζ-potential (mV)	−31	−19	+2	+20	+28

Supplementary data related to this article can be found at https://doi.org/10.1016/j.biomaterials.2020.120203.

2.3. Biofunctionalization of GUVs formed by droplet splitting microfluidic device

Despite the fact that charge-mediated cellular uptake of GUVs is an efficient process, it fails to provide a cell type-specific delivery of therapeutic compounds. Therefore, we aimed to introduce additional ligand-directed guidance for GUV uptake by developing a toolbox of strategies for bio-orthogonal functionalization of the GUV surface with specific targeting biomolecules. To exemplarily demonstrate the diversity of GUV biofunctionalization possibilities, we produced GUVs by microfluidic droplet splitting harboring a combination of three linkers: biotinylated lipids for coupling to streptavidin tagged proteins, NTA-Ni^{2+}-functionalized lipids for coupling to histidine-tagged proteins, and DOPE lipids containing primary ammine for linking to N-hydroxysuccimid (NHS)-functionalized molecules. We achieved triple orthogonal functionalization of the released GUVs by adding Atto425-labeled streptavidin, histidine-tagged green fluorescent protein and NHS-functionalized Alexa647 (Fig. 3a). Moreover, we tested more complex sequential functionalization strategies. Towards this end, we immobilized cysteine-functionalized gold nanoparticles to the GUV lipids *via* NHS-chemistry (Fig. 3b and Video S4). Additionally, we tested a multistep approach to couple immunoglobulins (*e.g.* anti-CD3) *via* NTA-immobilized His-tagged protein G (Fig. 3c). Of note, this approach was focused on coupling

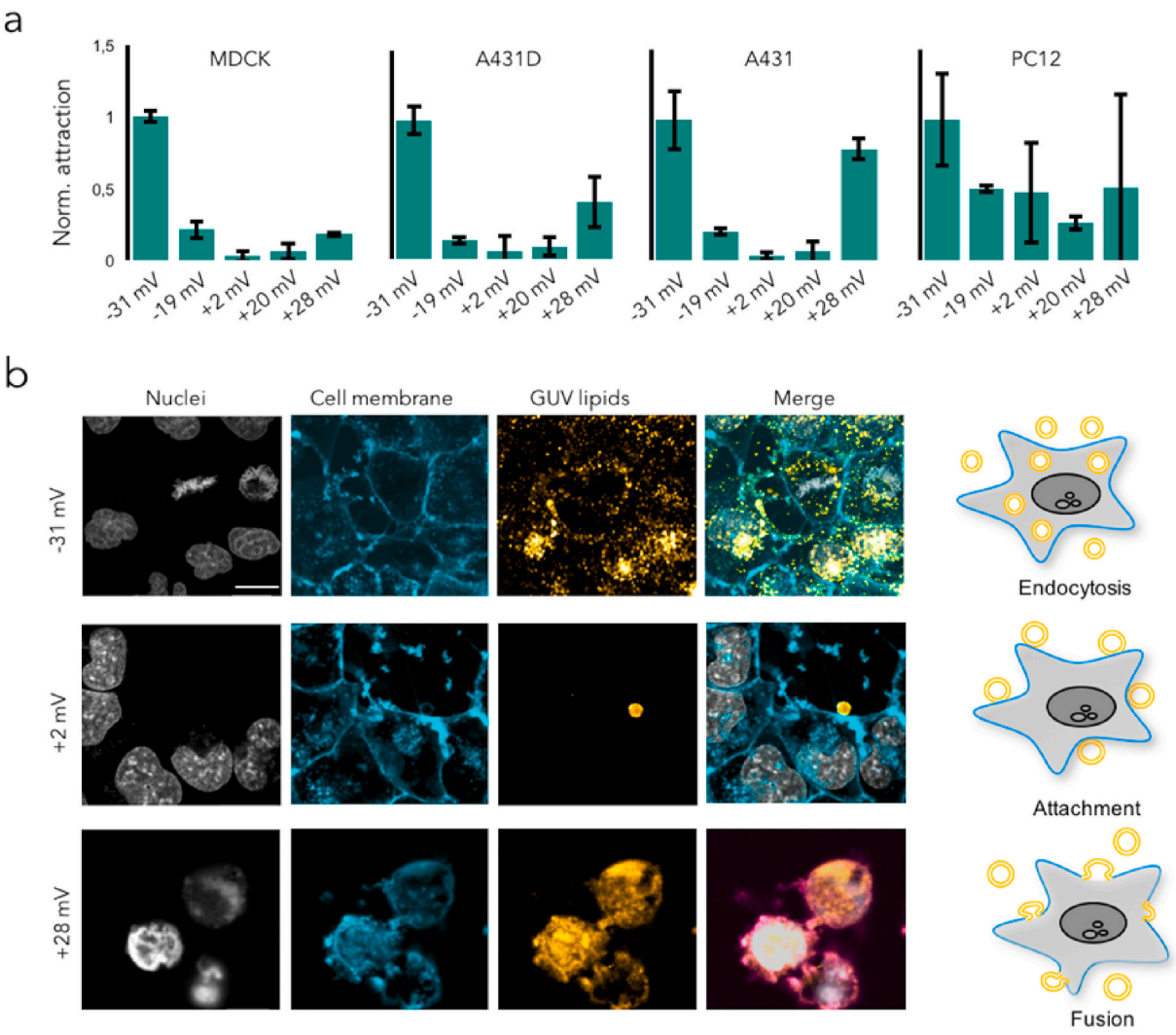

Fig. 2. Charge-mediated GUV-cell interactions. (a) Attraction quantification of differently charged GUVs (ζ-potential as indicated on x-axis) with cell lines of endothelial (MDCK), epithelial (A431D and A431) and adrenal (PC12) origin after 24 h of joint incubation (results are shown as average values normalized to −31 mV average and SD from three technical replicates). (**b**) Representative single plane fluorescence confocal microscopy images and schematic representation of charge-mediated GUV-A431D cell interactions after 24 h of joint incubation and several washing steps. Nuclei (first column) were stained with Hoechst 33342, cell membranes (second column) were stained with WGA-AlexaFluor488 and GUVs (third column) were visualized by incorporation of LissRhod-PE fluorescent lipids into GUVs. The respective GUV charge is indicated on the left side of the image. The scale bar is 20 μm. See Table S1 for details on the lipid and buffer compositions.

ligands of interest to the outer GUV leaflet. However, since the functional groups conjugated to the lipids are also exposed on the inner GUV leaflet, intraluminal coupling could also be explored in future studies.

Supplementary data related to this article can be found at https://doi.org/10.1016/j.biomaterials.2020.120203.

Notably, antibodies offer great selectivity for particular cell surface antigens, which is why antibody-based targeting has previously been shown to greatly enhance specific SUV delivery to defined cell subsets [30]. To assess the functionality of anti-CD3-coated GUVs, we incubated them with $CD3^+$ Jurkat cells (see Experimental Section). When analyzed by confocal microscopy, the formation of an attachment site between the GUVs and the cells, strikingly reminiscent of a "minimal" immunological synapse, was observed (Fig. 3d), indicating successful GUV-cell coupling. In contrast, GUVs without anti-CD3 coating did not show this complex interaction architecture.

To systematically assess the possibility of employing attractive, receptor-specific GUV-cell interactions for targeted GUV delivery, we produced negatively charged and RGD-biofunctionalized GUVs with varying ligand densities (Fig. 3e). We decided to use the RGD tripeptide for GUV biofunctionalization as integrin receptor-based endocytosis has previously been shown to enhance liposomal drug delivery due to the ability of integrin proteins to function as natural intracellular signal transducers for the initiation of endocytic events [31]. Therefore, we interfaced RGD-GUVs with adherent cell lines expressing RGD-binding integrin receptors and measured their attraction. As a control we incubated the same cells with non-functionalized, naive GUVs. For all cell lines tested (Fig. 3f), we found that RGD ligand density on the cell periphery correlates with GUV attraction. In addition, GUV-cell coupling can be increased by approximately 10% when applying 10 mol%-RGD ligand decoration. In the case of non-adherent Jurkat T-cells, that express high levels of $\alpha_4\beta_1$ integrin [32], 10 mol%-RGD coating increased GUV-cell coupling even 15-fold (as measured by fluorescence flow cytometry). We further analyzed the nature of the interaction between RGD-GUVs and cells by confocal microscopy. When interfaced with A431D cells, GUVs mostly accumulated at the cell periphery, the region with the highest integrin density, and in the perinuclear region, suggesting RGD-integrin-mediated endocytotic GUV uptake by the cells (Fig. 3g).

2.4. Regulating attractive and repulsive GUV-cell interactions for targeted delivery

Although biofunctionalization of GUVs with anti-CD3 and RGD ligands successfully increased GUV-cell interactions, charge-driven and other nonspecific attractions at the GUV-cell interface might still be

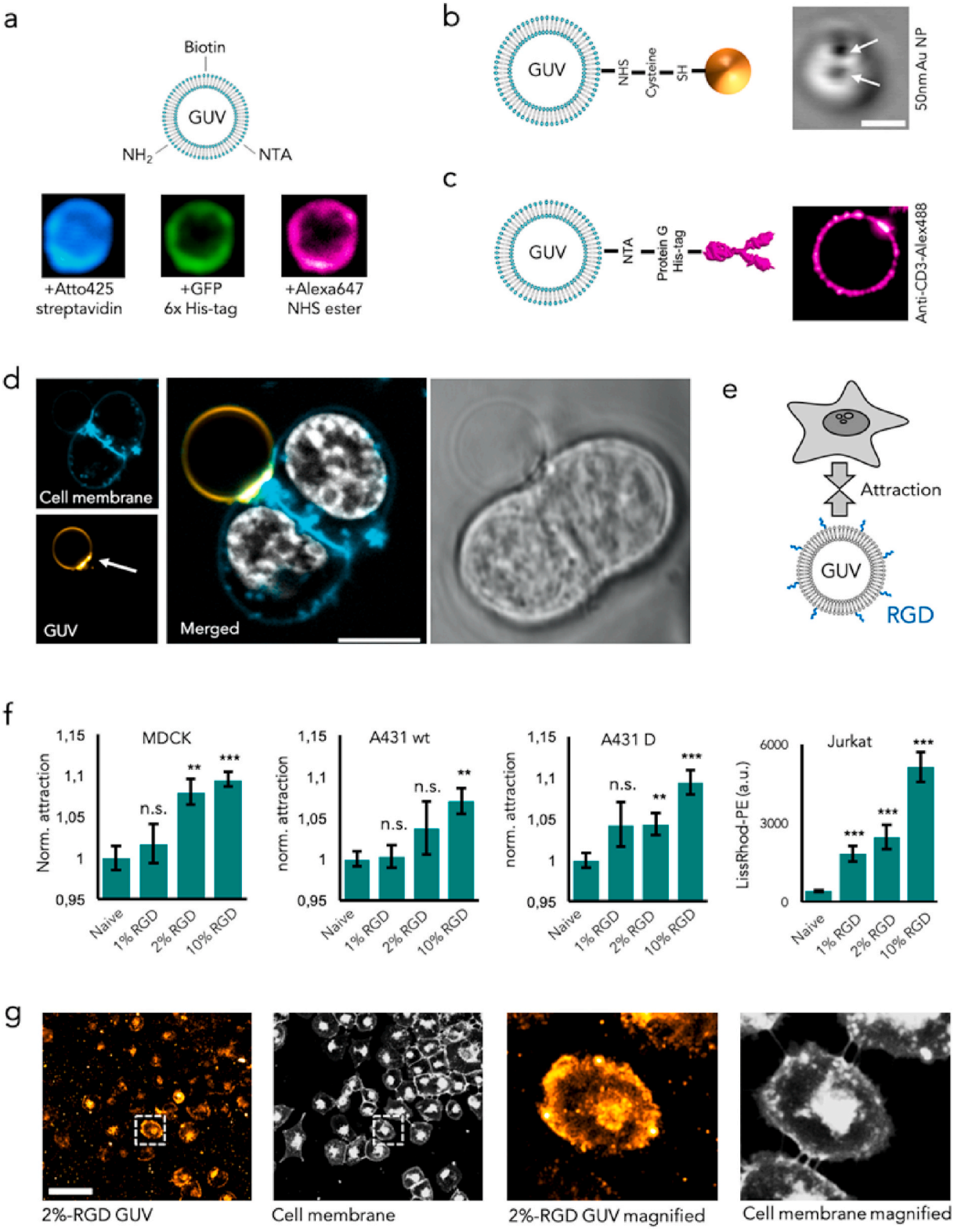

(caption on next page)

strong enough to interfere with ligand-based cell type-specific uptake. For example, when incubating non-charged GUVs functionalized with NrCAM proteins together with SH-SY5Y neuroblastoma cells, the measured attraction was comparable to that of non-functionalized, non-charged GUVs (Fig. S6). This indicates that the strength of nonspecific lipid-cell interactions is considerably high and can interfere greatly with ligand-based binding. Inspired by so-called "stealth" liposomes, which are commonly used for uptake studies using small vesicle (< 100 nm) [33], we set out to produce poly-ethylenglycol (PEG)-covered GUVs with the purpose of minimizing electrostatic and other non-specific interactions (Fig. 4a). Moreover, respective PEGylated vesicles are also known to exert reduced surface biofouling, providing increased interface stability and lower opsonin coating [34]. To characterize the shielding potential of PEG on GUVs of different charges, we

Fig. 3. Strategies for GUV biofunctionalization and receptor-specific GUV-cell interactions. (a) Schematic illustration and representative single plane fluorescence confocal microscopy images of fluorescently labeled, triple-functionalized GUVs produced by a droplet splitting microfluidic device. The fluorescence labels, Atto425-streptavidin, His-tagged GFP and NHS-Alexa647, were linked to NTA-Ni^{2+}, biotin and NH_2-conjugated lipids, respectively. (**b** and **c**) Schematic representations and microscopy images of sequential GUV functionalization with 50 nm gold nanoparticles (**b**) and antibodies (**c**). Right panels show a phase contrast image of GUVs linked to a gold nanoparticle (indicated by white arrows) and a fluorescence confocal image of GUVs functionalized with AlexaFluor488-linked Anti-CD3 IgG-immobilized *via* His-tagged ProteinG to NTA-Ni^{2+} lipids (c). Scale bars are 1 μm and 2 μm for (b) and (c), respectively. (**d**) Formation of an interaction area between anti-CD3-functionalized GUVs and $CD3^+$ Jurkat T-cells after incubation for 24 h. Cell membranes were stained with WGA-AlexaFluor488 (top left image), GUVs were visualized by incorporation of LissRhod-PE fluorescent lipids (bottom left image) and nuclei in the merged image were stained with Hoechst 33342 (middle). The arrow indicates the site of lipid clustering at the GUV-cell interface. The right image shows the respective bright field image. The scale bar is 6 μm. (**e**) Schematic representation of GUV decoration with integrin-specific RGD ligands to induce integrin-mediated attractive interactions at the GUV-cell interface. (**f**) Attraction analysis of RGD-functionalized GUVs incubated with different cell lines. The presented results are normalized to the attraction of naive GUVs, and shown as average value and SD from three technical replicates. Attraction of RGD-functionalized GUVs to Jurkat cells in suspension was assessed by flow cytometry. T-test with ** = $p < 0.001$, *** = $p < 0.0001$, n.s. not significant to the naïve vesicles treatment group in each graph. (**g**) Representative fluorescence confocal microscopy images of fluorescently labeled GUVs (LissRhod-PE) decorated with 2 mol% RGD ligands incubated with membrane-stained (WGA-AlexaFluor488) A431D cells. The scale bars are 60 μm. The areas surrounded by dashed borders are shown in greater magnification in the two images on the right. The accumulation of GUVs at the cell periphery and in the perinuclear region after incubation of 24 h is visible. See Table S1 for details on the lipid and buffer compositions.

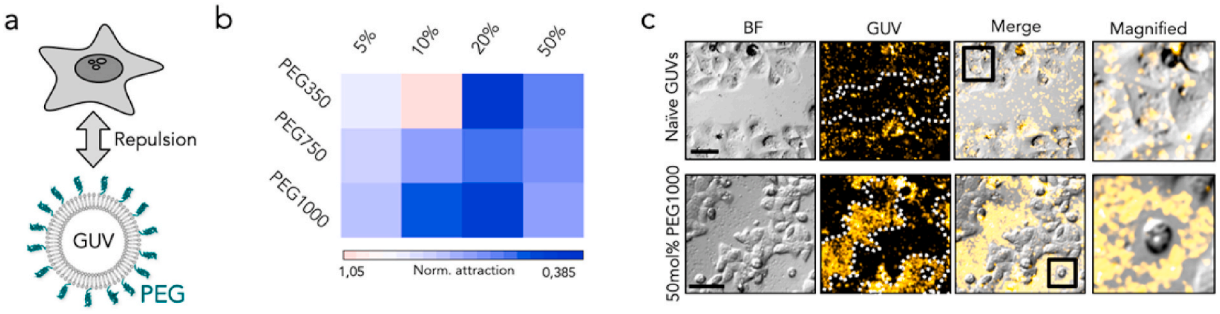

Fig. 4. Regulating attractive and repulsive GUV-cell interactions. (a) Schematic representation of the PEG-functionalized GUVs created to suppress non-specific charge-mediated GUV-cell interactions that interfere with ligand-specific GUV-cell interactions. (**b**) Heat map of the attraction analysis of PEG-functionalized GUVs that contain 50 mol% negatively charged lipids and are interfaced with Hela cells. (**c**) Representative bright field (first column) and fluorescence (second column) confocal microscopy images of A431 cells interfaced with naive, negatively charged GUVs (top row) or 50 mol% PEG1000-functionalized, negatively charged GUVs (bottom row). Naive GUVs are in direct contact with the cells while PEGylated GUVs accumulate in the intercellular space (merged image, third column) and form contact inhibition zones with the cells (the fourth column shows magnified images of the areas indicated by a black box in the merged images). White dotted lines indicate the periphery of cell groups deduced from the bright field image. Scale bars are 15 μm. See Table S1 for details on the lipid and buffer compositions.

produced GUVs containing either 15 or 50 mol% negatively and positively charged lipids. We then tested a series of concentrations (5, 10, 20 and 50 mol%) of lipids linked to PEG with different molecular weights (PEG350, PEG750 or PEG1000). Importantly, we did not observe any prominent difference in dsGUV formation when applying SUVs harboring PEG350 and PEG750 conjugated lipids. However, for SUVs containing 20 mol% and 50 mol% PEG1000 lipids, a reduced dsGUV formation was observed, probably due to charge-shielding effects between the PEGylated SUV surface and the droplet periphery. In a first step, we measured the ζ-potential of respective SUVs before dsGUV production and the ζ-potential of the released GUVs (Fig. S7a). The results reveal that the ζ-potential of both negatively and positively charged vesicles decreases with increasing length of the PEG chain and the rate of PEGylation. In a second step, we tested whether PEGylation of the GUVs and the associated masking of the GUV surface charge, results in the creation of a repulsive interaction between GUVs and cells. Towards this end, we incubated PEGylated GUVs with six different cell lines established from different tissues and measured the respective GUV attraction (Fig. S7b). The results revealed that for all tested cell lines, GUV PEGylation decreased charge-mediated attraction between the GUVs and the cells. Moreover, this effect was more pronounced in cases of higher PEGylation rates and longer PEG length. For example, in the case of GUV interactions with A431D carcinoma cells, GUVs equipped with 5 mol% PEG350 showed almost 50% more attraction compared to GUVs equipped with 50 mol% PEG350 (Fig. 4b). Consistently, confocal microscopy analysis showed that naive, negatively charged GUVs were usually localized within or above cells and only a small fraction was found between single cells or cell groups (Fig. 4c top panel). In contrast, PEGylated GUVs were observed mostly accumulating in the intercellular space, forming contact inhibition zones between accumulations of GUVs and individual cells (Fig. 4c bottom panel). Most probably, this behavior can be attributed to repulsive GUV-cell interactions.

With the ultimate goal of developing a fine-tuned means for targeted uptake of GUVs into specific cells, we developed complementary strategies that decrease distorting, nonspecific, electrostatic attractive interactions between cells and GUVs through PEG-based passivation, and promote specific interactions through GUV biofunctionalization using cell type-specific ligands.

To this end, we combined the strategies of PEGylation and biofunctionalization of GUVs and completed a screen for cell type selectivity. To achieve that, we produced GUVs consisting of 20 mol% negatively charged EggPG lipids, 54 mol% neutral EggPC lipids, 20 mol % PEG750-linked lipids, 5 mol% LissRhod PE and 1 mol% NHS-coupled lipids for ligand immobilization. In this lipid composition, the net strength of ligand-receptor interactions between the GUV and the target cell needs to be strong enough to overcome PEG-mediated repulsion, eventually allowing cell type-specific endocytosis induced by the negative GUV charge (Fig. 5a). To assess the specificity, we first screened 15 types of differently functionalized GUVs, each of which we expected to be either specific for a given cell type (*e.g.* anti-cadherin antibodies or bradykinin) or nonspecific (*e.g.* poly-L-lysine) and measured respective attraction values for six different carcinogenic cell lines. Respective carcinogenic cells might resemble potentially interesting targets for GUV-based tumor treatment. In order to reference all attraction values for each cell type to a common, moderately unreactive protein, all values obtained were normalized to the attraction value determined for BSA-coupled GUVs (Fig. S8). Fig. 5b shows the attraction values between the six differently functionalized GUVs and six cell lines of different origin. GUVs coated with peptides and proteins which do not

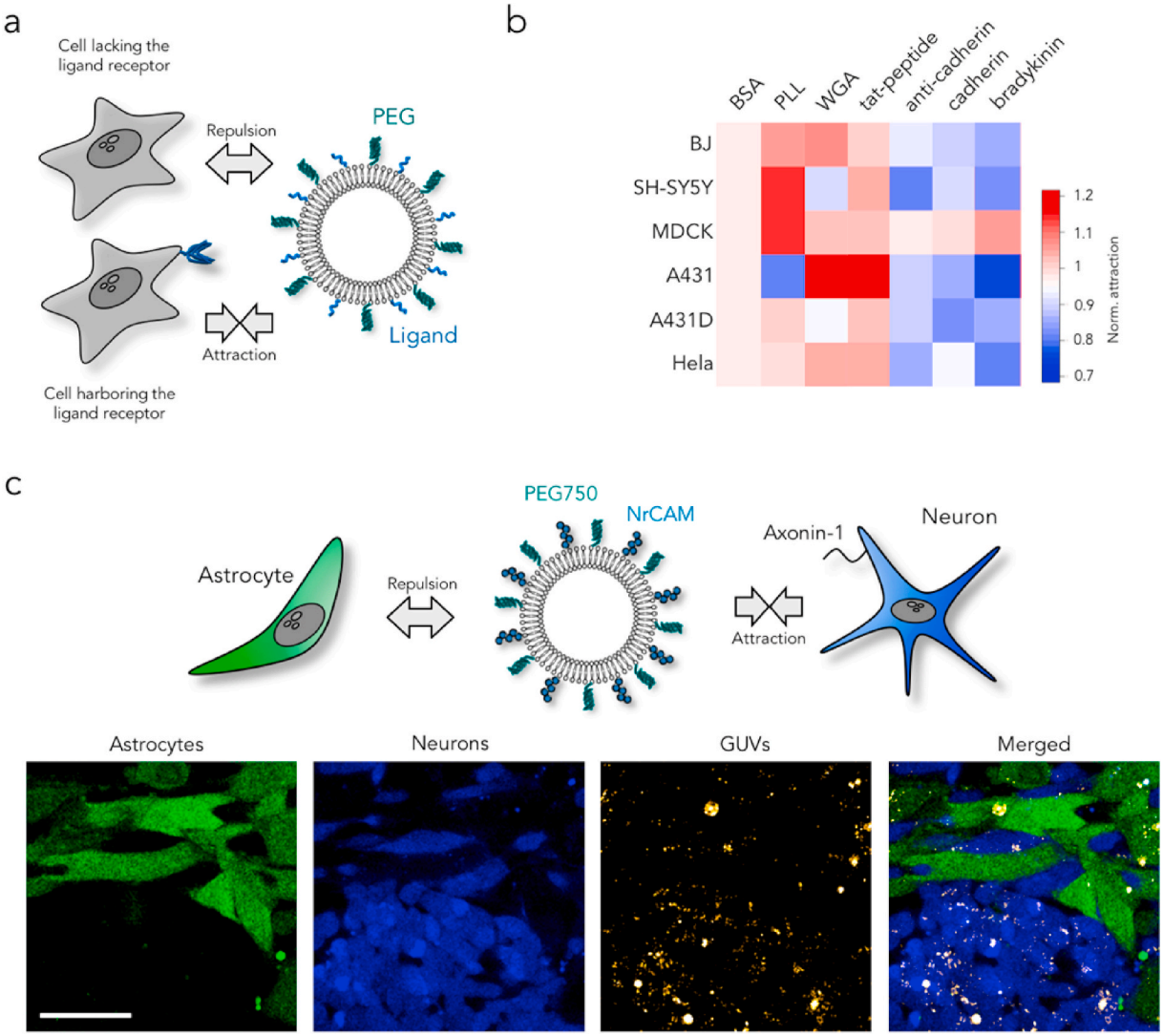

Fig. 5. Specific GUV-cell interactions. (a) Schematic representation of a PEGylated GUV biofunctionalized with receptor specific ligands to achieve specific attraction between GUVs and the respective receptor-expressing cell. (**b**) Attraction values of nonspecific (i.e., BSA, PLL, WGA and tat-peptide) and specific (i.e., anti-cadherin, recombinant cadherin and bradykinin) protein-biofunctionalized GUVs (*via* 5 mol% NHS lipids and 20 mol% PEG750) to human fibroblast BJ cells, neuroblastoma SH-SY5Y cells, endothelial MDCK cells, epithelial A431 cells, dexamethasone-treated epithelial transformed A431 cells and Hela cells. All values were normalized to the attraction of BSA-coupled GUVs. (**c**) Schematic representation of PEGylated GUVs biofunctionalized with NrCAM in a co-culture with astrocytes and neuronal cells, which lack and express the axonin-1 receptor, respectively. The bottom panel shows representative single plane confocal microscopy images of the co-culture of astrocytes (green) and neurons (blue) following 24 h of incubation with NrCAM-biofunctionalized, 20 mol% PEG750 conjugated GUVs. Hs683 astrocytes and SH-SY5Y neurons were stained with CellTracker Green and Blue, respectively. GUVs were visualized by incorporation of LissRhod-PE fluorescent lipids. The scale bar is 50 μm. See Table S1 for details on the lipid and buffer compositions.

bind to cells in a specific manner – *e.g.* poly-L-lysine (which mostly interacts based on electrostatic interaction), wheat germ agglutinin (WGA, which binds to the glycocalyx of cells), or HIV derived tat-peptide (an arginine-rich peptide which penetrates cell membranes mostly based on hydrophobic interactions) – showed high attraction to basically all cell types, as the nonspecific attractions were able to overcome the repulsive PEG-barrier in all cases. When targeting more specific receptors, e.g., bradykinin-specific G-protein-coupled receptors (abundantly expressed on epithelial cells) by functionalizing GUVs with the vasodilator bradykinin, we achieved specific attraction to endothelial cells. In this case, specific attraction was increased up to 40% compared to other cell lines. Similar results were obtained when targeting cadherin proteins by coating with recombinant cadherin or anti-cadherin antibodies. This comparison shows that the fine-tuning of specific attractive interactions and the use of PEG-based shielding of non-specific interactions is a well-suited strategy to target GUVs to specific cells4

Finally, to assess whether our strategy for guided attraction is able to induce a cell-type specific uptake of GUVs in a more complex multi-cell type environment, we tested our GUV targeting approach in co-culture experiments. Towards this end, we chose astrocyte (Hs683) and neuronal (SH-SY5Y) model cell lines, as these cell types grow and interact in great proximity in the mammalian brain. Moreover, achieving preferential GUV uptake by neurons is desirable when developing therapeutic strategies for neuroblastoma or neurodegenerative diseases. To test the guided attraction, we prepared GUVs composed of 20 mol% PEG750, 20 mol% EggPG, 58 mol% EggPC, 1 mol% LissRhod PE and 1 mol% 18:1 DGS-NTA(Ni) lipids and functionalized these with the neuronal adhesion molecule His-tagged NrCAM (extracellular domain aa20 - 630) which binds to axonin-1 on neuronal membranes (Fig. 5c) [35]. Following 24 h of co-culturing the two cell types with GUVs, we performed confocal microscopy to analyze and quantify the interaction of the GUVs with each cell type from respective images (see Experimental Section). The analysis revealed that neuronal cells contained up

to 520% more GUVs compared to astrocytes, highlighting the importance of fine-tuning attractive and repulsive interaction for targeted delivery of GUVs in a complex environment.

2.5. Lysosomal escape of the GUV cargo for cytoplasmic delivery

To investigate the mechanism of intracellular GUV uptake, we incubated negatively charged GUVs with REF cells stained for endosomal vesicles and cytoplasm. Confocal microscopy of the respective cultures revealed that incorporated GUVs are surrounded by endosomal membranes (Fig. 6a). This observation confirms that GUVs enter into the cells by endocytic pathways (*e.g.* micropinocytosis or phagocytosis), excluding other uptake mechanisms such as direct penetration or sole engulfment of the GUVs. However, following uptake, we observed a progressive loss of GUV fluorescence over time. After 24 h of incubation, fluorescence was found to co-localize with LysoTracker Green DND-26 stained organelles (Fig. 6b). This observation might be attributed to successive lysosomal degradation of the vesicles, a process frequently observed for SUV-based delivery methods. Yet because many pharmacological compounds target cytoplasmic components, efficient lysosomal escape mechanisms that allow for the release of GUV cargo into the cell and avoid lysosomal degradation are a pivotal requirement for such applications [36,37].

To circumvent lysosomal degradation, we assessed three independent lysosomal escape mechanisms, all of which are based on the sudden decrease in pH occurring during endosome-lysosome fusion: 1) Lysosomal escape *via* a proton sponge mechanism based on the incorporation of high molecular weight poly-ethylene-imine (PEI) into the GUVs [38]; 2) Lysosomal escape *via* intra-lysosomal membrane fusion and pore formation by attachment of the pH-sensitive GALA peptide onto the GUV surface [39]; 3) Lysosomal escape *via* intra-lysosomal fusion by incorporation of the pH-sensitive lipid DOBAQ into the GUV membrane [40]. We exemplarily assessed the retention, degradation and release of GUV cargo by loading the GUVs with the membrane impermeable dye HPTS and observing its intracellular fluorescence distribution after 24 h of incubation of the respective GUVs with A431D cells (Fig. 6c). In the cases of PEI-loaded and GALA-coupled GUVs, HPTS fluorescence was exclusively detected in punctuated form, co-localizing with fluorescence originating from the GUVs inside the cells. This indicates HPTS retention inside the GUVs and, therefore, endosomal or lysosomal entrapment, suggesting unsuccessful cytoplasmic cargo release. However, in the case of GUVs containing 60 mol% DOBAQ, HPTS fluorescence was found distributed throughout the entire cell body, thus proving successful release of HPTS from the GUVs into the cytoplasm. Indeed, DOBAQ-containing GUVs show polarity switching of their ζ-potential at low pH, as assessed by dynamic light scattering (Fig. S9).

The dynamics of endocytosis and lysosomal activity can significantly vary between transformed and untransformed cells, therefore we aimed to also test our approach on primary cells [41,42]. For these

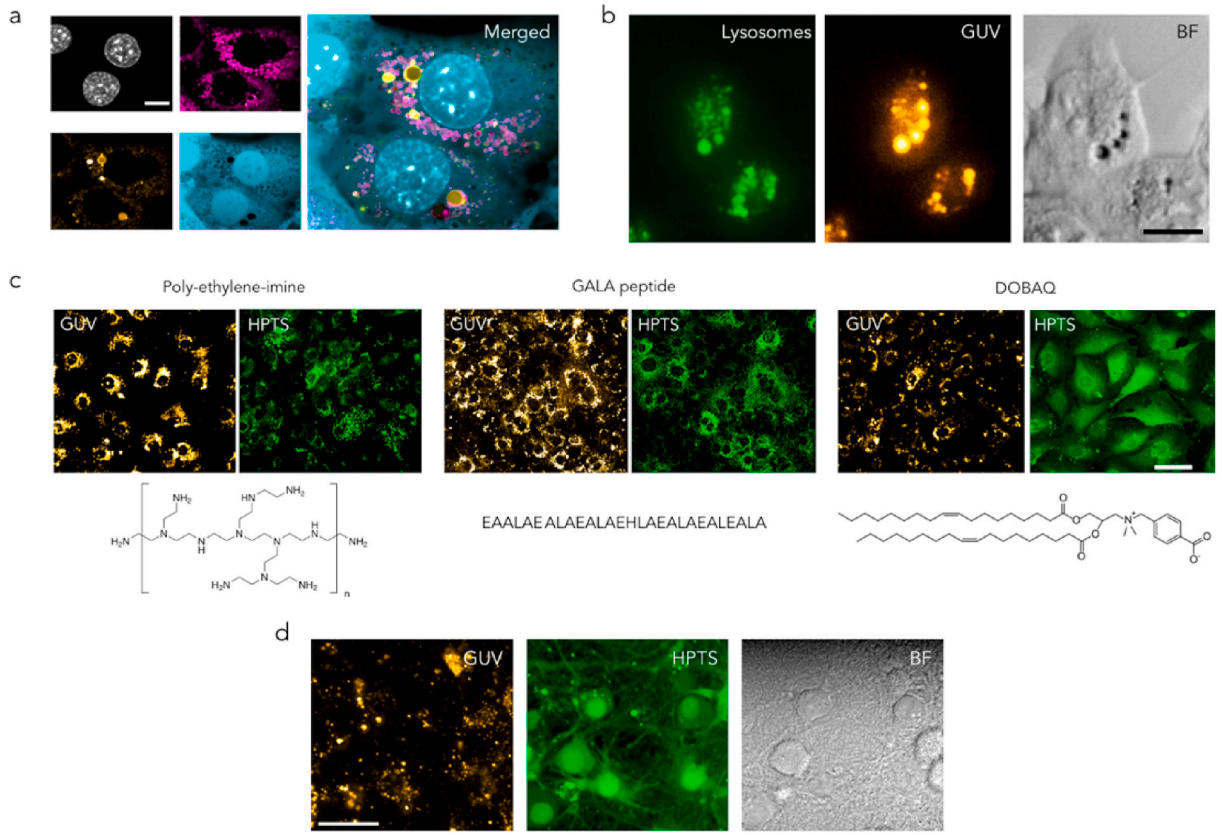

Fig. 6. Lysosomal degradation of the vesicles and the assessment of the mechanisms for lysosomal escape to allow intracellular GUV cargo release. (a) Representative fluorescence confocal microscopy images of REF cells loaded with endosomal entrapped, negatively charged GUVs. Nuclei (top left image) were stained with Hoechst 33342, endosomes (top center image) were labeled by staining with WGA-AlexaFluor488 for 24 h, GUVs (bottom left image) were visualized by incorporation of LissRhod-PE fluorescent lipids, and cytoplasm (bottom center image) was stained using CellTracker Green. The merged image (right image) shows that GUVs reside within the cytoplasm and are entrapped in endosomal vesicles. The scale bar is 10 μm. (**b**) Representative fluorescence microscopy images of REF cells showing co-localization of GUVs with lysosomal compartments after 24 h of incubation. Lysosomes (left panel) were stained with LysoTracker Green and GUVs (center panel) were visualized by incorporating LissRhod-PE fluorescent lipids. The right panel shows bright field images. The scale bar is 10 μm. (**c**) Representative fluorescence confocal microscopy images of the assessment of PEI-, GALA peptide- and DOBAQ-mediated lysosomal escape for HPTS(green)-loaded GUVs (yellow) incubated with REF cells for 24 h. The scale bar is 50 μm. (**d**) Representative fluorescence confocal microscopy and bright field images of primary mouse hippocampal neurons (right panel) incubated with GUVs (left panel, visualized by incorporation of 1 mol% LissRhod PE lipids) loaded with HPTS (center panel) and containing 60 mol% of the pH-sensitive lipid DOBAQ. The scale bar is 30 μm. See Table S1 for details on the lipid and buffer compositions.

experiments, we used *in vitro* cultured primary hippocampal neurons [43], cells that represent an important target in many therapeutic procedures treating neurodegeneration or neuronal tumors. When interfaced with HPTS-loaded and DOBAQ-containing negatively charged GUVs, we observed extensive uptake of the GUVs into the neurons after 24 h of incubation (Fig. 6d). In order to enhance their attraction to the sialic acid-containing glycocalyx, the GUVs were functionalized with WGA. Their accumulation in the perinuclear region suggests incorporation into the cell's intracellular trafficking machinery. Importantly, we observed widespread distribution of HPTS fluorescence within the neuronal soma and in the dendrites. This observation proves that DOBAQ-based lysosomal escape of GUV cargo is functional and compatible with primary cells.

2.6. Delivery of very large complex cargo

To ultimately assess the cargo capacity of GUVs formed by microfluidics for novel therapeutic approaches, we performed microfluidic loading of purified virions formed by baculovirus (BV). BV is a non-human, arthropod specific enveloped virus comprising a double-stranded DNA genome ~140 kb in size, characterized by a flexible capsid which can accommodate very large (exceeding 100 kb) additional heterologous DNA insertions. The membrane envelope of BV can be engineered to alter the tropism of this originally insect-cell specific virus, converting BV into a non-replicative, non-integrating tool for delivering complex DNA circuitry into mammalian cells, tissues and organisms [44,45]. Due to its very large DNA capacity, combined with the ease of manufacture and engineering, BV is emerging as a promising tool for genome engineering approaches in gene and cell therapy, potentially as a replacement technology for current viral vector systems (adenovirus, adeno-associated virus, lentivirus) [46]. We reasoned that the potential of BV could be maximized, ultimately for *in vivo* applications, by utilizing GUVs to transport and protect defined ensembles of BVs to target cells and tissues of choice. By using our microfluidics approach, we achieved successful assembly and release of BV-loaded GUVs (Fig. 7a). Next, the BV-loaded DOBAQ-containing GUVs were incubated with REF cells for 24 h. By confocal microscopy we observed intracellular uptake of the GUVs, as well as release of the BV (stained by Hoechst 33342, see Experimental Section) into the cell cytoplasm (Fig. 7b). This was accompanied by the expression of mitochondrial targeted dsRed protein encoded by the BVs, indicating successful GUV based transduction of mammalian cells with BV carrier GUV. Moreover, quantification of the dsRed fluorescence in cultures treated with GUV-entrapped BVs and soluble BVs showed that GUV-based intracellular delivery of the virions can significantly augment the expression of exogenious BV-encoded genes (Fig. S10). These results highlight the advantages of GUV-based drug delivery towards more efficient drug administration of very large complex cargo, here entire BVs, that would not be possible by conventional SUV-based delivery.

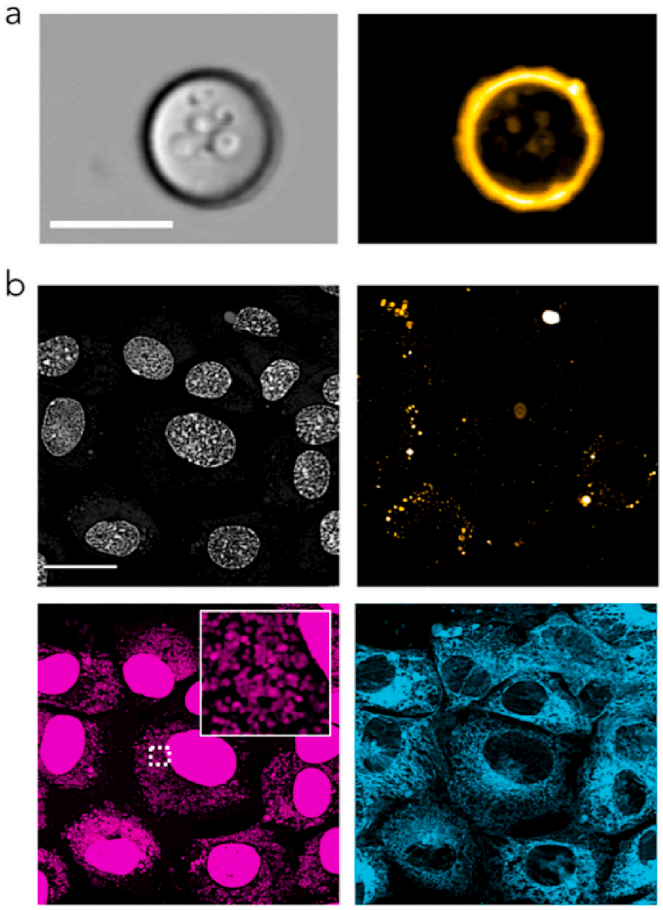

Fig. 7. GUV-based delivery of heavy duty and complex cargo. (a) Representative bright field (left panel) and corresponding confocal microscopy (right panel) images of a BV-loaded GUV. The scale bar is 2 μm. (**b**) Maximal z-projection of fluorescence confocal microscopy images of REF cells (nuclei stained with Hoechst 33342, top left image) that were incubated for 24 h with baculoviruses (bottom left image, visualized by oversaturation of the Hoechst 33342 channel) that had been loaded into DOBAQ-containing GUVs (top right image). Note the visible expression of mitochondria-targeted dsRed (bottom right image). The scale bar is 25 μm. See Table S1 for details on the lipid and buffer compositions.

3. Summary and outlook

In this study, we developed a high-throughput droplet-based microfluidic production pipeline for producing large amounts of well-defined carrier-GUVs (d ≈ 2 μm) for drug delivery purposes. The presented technology is based on three subsequent steps: 1) well-controlled assembly of dsGUVs; 2) dsGUV mechanical splitting; and 3) the release of fully equipped GUVs into a physiological environment. This sequential assembly approach allows for highly efficient cargo loading and unprecedented control over the biological and physicochemical properties of the GUVs membranes. The ability to control GUV properties – specifically control over size, cargo, robustness during handling as well as specificity and strength of interactions – in such a precise manner has allowed us to perform a systematic assessment of key factors that dominate GUV-cell interactions and to explore concepts for targeted GUV delivery. We conceptually show how charge-driven as well as specific ligand-receptor-based attractive interaction between GUVs and cells can be utilized for regulating uptake. Moreover, we present a systematic evaluation of how PEG decoration of GUVs, which creates repulsive interactions can be employed to decrease nonspecific, electrostatic interactions and boost targeting specificity. We further describe a simple but efficient cytoplasmic release strategy for GUV cargos, based on the pH-sensitive lipid DOBAQ. The exquisite control over the GUV composition as well as the described GUV functionalization strategies allow for the construction of GUVs with an excessive functional diversity and high targeting specificity.

Our results with BV-loaded GUVs compellingly demonstrate that our approach could be applied in the future for transporting and delivering very large, complex cargo to cells and tissues of choice. Freights could include ensembles of viruses with multiple genome engineering modalities, or drug releasing porous microparticles, unprecedented quantities *in vivo* imaging probes, DNA origami robots and other biological and synthetic nanodevices or combinations thereof. In this case, the GUV shell could not only allow for targeted transport, but also prevent cargo degradation inside the GUV lumen. Moreover, by functionalizing the GUV surface, potentially immunogenic cargo could be shielded from immune reactions. Once the GUV arrived at its destination, the cargo would then be intracellularly discharged *via* the lysosomal escape mechanism. The mechanical stability of droplet-splitted GUVs could in future be further increased by their coating with stabilizing polymers and/or sugars. Such mechanically more robust GUVs,

could then pave the way for long lasting blood circulation or other *in vivo* application which require high mechanical stability. This study, characterizing GUV-cell interactions and GUV guidance, lays the foundation for such highly promising future applications. Moreover, our investigation of GUV-cell interactions will prove useful for bottom-up synthetic biology approaches, aiming to create novel systems in between living and synthetic cells. Here, interaction within hybrid tissues and therefore the micro- and mesoscale architecture of these, could be controlled using the concepts presented in this study.

4. Experimental Section

4.1. Materials

EggPG L-α-phosphatidylglycerol (Egg, Chicken), EggPC L-α-phosphatidylcholine (Egg, Chicken), 18:1 DOPG 1,2-dioleoyl-sn-glycero-3-phospho-(1′-rac-glycerol), 18:1 DOPC 1,2-dioleoyl-sn-glycero-3-phosphocholesteroline, 18:1 DOPE 1,2-dioleoyl-sn-glycero-3-phosphoethanolamine, LissRhod PE 1,2-dioleoyl-sn-glycero-3-phosphoethanolamine-N-(lissamine rhodamine B sulfonyl), 18:1 DGS-NTA(Ni) 1,2-dioleoyl-sn-glycero-3-[(N-(5-amino-1-carboxypentyl)iminodiacetic acid)succinyl] (nickel salt), 18:1 DOTAP 1,2-dioleoyl-3-trimethylammonium-propane, 18:1–12:0 Biotin PE 1-oleoyl-2-(12-biotinyl-(aminododecanoyl))-sn-glycero-3-phosphoethanolamine, DSPE-RGD 1,2-distearoyl-sn-glycero-3-phosphoethanolamine-N-[4-(p-(cysarginylglycylaspartate-maleimidomethyl)-cyclohexane-carboxamide], 18:1 PEG350 PE 1,2-dipalmitoyl-sn-glycero-3-phosphoethanolamine-N-[methoxy (polyethylene glycol)-350], 18:1 PEG750 PE 1,2-dioleoyl-sn-glycero-3-phosphoethanolamine-N-[methoxy(polyethylene glycol)-750], 18:1 PEG1000 PE 1,2-dioleoyl-sn-glycero-3-phosphoethanolamine-N-[methoxy (polyethylene glycol)-1000], and extrude set with 50 nm pore size polycarbonate filter membranes were purchased from Avanti Polar Lipids, USA. All lipids were stored in chloroform at −20 °C and used without further purification. DyLight 405 NHS Ester, AlexaFluor 647-NHS, Anti CD3 (16-0038-81), Anti CD3-Alexa488 (53-0037-42), Hydroxypyrene-1,3,6-trisulfonic acid trisodium salt (HPTS), Hoechst 33342, CellTracker Blue CMAC dye, CellTracker Green CMFDA dye, LysoTracker Green DND-26 dye, wheat germ agglutinin (WGA)-AlexaFluor conjugates, Dulbecco's Modified Eagle Medium (DMEM) high Glucose, 1:1 DMEM:F12, RPIM-1640, FluoroBrite DMEM (high glucose), heat inactivated fetal bovine serum, penicillin-streptomycin (10,000 U/mL), GlutaMax Supplement, L-Glutamine (200 mM), trypsin-EDTA (0.05%) with phenol red, phosphate buffered saline, basic fibroblast growth factor (aa 10–155), Epithermal growth factor, AlexaFluor405 dye and custom synthesized GALA peptide (EAALAE ALA-EALAEHLAEALAEALEALA) were purchased from Thermo Fischer Scientific, Germany. NHS Palmitic acid N-hydroxysuccinimide ester, 97% L-cysteine, 50 nm Au nanoparticles, heat-inactivated horse serum, lectin (Wheat Germ Agglutinin), 1H,1H,2H,2H-Perfluoro-1-octanol (PFO) de-emulsifier, bradykinin, polyethylenimine (branched, Mw ~25,000), Atto425-Biotin, human Interleukin 2, recombinant insulin, fibronectin from bovine plasma, poly-L-lysine and DOBAQ N-(4-carboxybenzyl)-N,N-dimethyl-2,3-bis(oleoyloxy) propan-1-aminium were purchased from Sigma Aldrich, Germany. Polydimethylsiloxan (PDMS) Sylgard 184 was purchased from Dow Corning, USA. Protein G His-tag was purchased from BioVision, USA. Bovine albumin fraction V (BSA) was purchased from Carl Roth, Germany. His-tagged NrCAM 8425-NR-050 and human recombinant cadherin were purchased from R&D Systems, USA. Fluoresbrite YG Microspheres 1.00 μm were purchased from Polysciences Europe, Germany. Perfluoropolyether-polyethylene glycol (PFPE-PEG) block-copolymer fluorosurfactant was purchased from Ran Biotechnologies, USA. Anti-VE-Cadherin and anti-alpha4-integrin (CD49d) antibodies were purchased from Santa Cruz (Sc-28644) and Millipore (MAB1383). Recombinant human CD95L was purchased from BioLegend, USA. A431, Hela, Hs386, SH-SY5Y and Jurkat cell lines were obtained from ATCC, USA. REF52 cell lines [47] were a generous gift from Prof. Benjamin Geiger (Weizmann Institute, Rechovot). PC12 cells were a generous gift from Amin Rustom (Institute for Neurobiology, Heidelberg). Primary mouse hippocampal neurons were obtained from the Institute of Neurobiology, Interdisciplinary Center for Neurosciences in Heidelberg, Germany. Purified baculovirus specimens were obtained from Martin Pelosse (Commissariat à l'énergie atomique et aux énergies alternatives, CEA Grenoble, France). Tat-HIV-GFP peptides were a generous gift from Rüdiger Arnold (Life Science Lab, German Cancer Research Center).

4.2. Microfluidic-based GUV production

For the production of dsGUVs, SUV solution using the lipid compositions given in Table S1 were mixed as described previously [22,23]. Briefly, lipids dissolved in chloroform were mixed at respective ratios in glass vials and dried under a gentle nitrogen stream. The dried lipid films were rehydrated to a final lipid concentration of 3 mM in production buffers given in Table S1 for 30 min. Subsequently, the solution was shaken for 5 min at min. 600 rpm. The resulting liposome solution was extruded at least 9 times through a 50 nm pore size polycarbonate filter. SUVs solutions were stored at 4 °C for up to 3 days or used for dsGUV production immediately.

Droplet-based microfluidic mechanical splitting devices were fabricated from PDMS. The devices were produced as previously described using photo- and soft-lithography methods [48]. Flow rates were controlled by an Elveflow OB1 MK3-microfluidic flow control system. If not stated otherwise, for the formation of GUVs within microfluidic droplets the SUV solutions were diluted to a final lipid concentration of 1.5 mM. For droplet formation, the SUV solutions were introduced into the aqueous channel of the microfluidic devices. Negatively charged GUVs were formed using 1.25 mM $PFPE_{(7000\ g/mol)}$-$PEG_{(1500\ g/mol)}$-$PFPE_{(7000\ gr/mole)}$ triblock surfactant dissolved in FC-40. Positively charged GUVs were formed using 0.5% RAN Biotechnologies PEG-based fluorosurfactant diluted in FC-40. For formation of GUVs containing DOBAQ lipids for lysosomal escape, 1.25 mM $PFPE_{(2500\ g/mol)}$-$PEG_{(600\ g/mol)}$-$PFPE_{(2500\ g/mol)}$ triblock surfactant diluted in FC-40 was used. Note that the addition of certain amounts of PFPE-COOH might be neccessary due to batch-to-batch variations in the surfactant purity. An aqueous to oil phase ratio of approximately 1:4 was used for all droplet productions. Droplets were formed at the flow-focusing junction of the splitting devices and collected from the outlet of the microfluidic chip into a microtube. Following collection, dsGUV were allowed to equilibrate for a minimum of 2 h at 4 °C before release.

For the release of dsGUVs from the oil phase and the stabilizing polymer shell, the excess oil phase was removed from the microtube. The droplet layer was mixed in a volume ratio of 1:1:1 (aq. production buffer: aq. Release buffer (see Table S1): destabilizing PFO). Following 30 min of equilibration, the GUV-containing aqueous phase was transferred into a 2 mL microtube. Release buffer was added to a total volume of 2 mL and GUVs were centrifuged at > 10.000 g for 15 min. The supernatant was discarded and the pellet was suspended to obtain the desired concentration.

4.3. Dynamic light scattering

Zeta potentials of GUVs and SUVs were measured with a Malvern Zetasizer Nano ZS system at a total lipid concentration of 15 μM in PBS. Equilibration time was set to 600 s at 25 °C, followed by three repeat measurements for each sample at a scattering angle of 173° using the built-in automatic run-number selection. The material refractive index was set to 1.42 [49] and solvent properties to $\eta = 0.8882$, $n = 1.33$ and $\varepsilon = 79.0$. For GUV zeta-potential measurements, equilibration time and number of individual measurements were set to 120 s and 2 repeats, respectively. The zeta-potential of DOBAQ-containing GUVs was assessed by diluting GUVs to a final lipid concentration of 15 μM in PBS adjusted to the desired pH by adding 4 N NaOH or 10% HCl. All zeta-potential measurements were performed at least in duplicates.

4.4. Assessment of droplet homogeneity

To assess transmission heterogeneity of intraluminal droplet contents, w/o droplets were produced at a flow-focusing junction of either

a droplet splitting device or a simple droplet production device. A PBS aqueous phase containing 10 mM $MgCl_2$, 1 mM AlexaFluor405, 1 μM His-tagged GFP, 1.08×10^9 particles/mL Fluoresbrite YG Microspheres (D = 1.00 μm) was used. Droplets were collected and mean droplet fluorescence intensity for all fluorophores was measured from single plane fluorescence confocal images using global thresholding segmentation and the ImageJ particle analyzer.

4.5. Quantitative mass spectrometry

For quantitative mass spectrometry analysis of SUV and GUV lipid content, GUVs were produced from the SUVs composed of 33 mol% DOTAP, 33 mol% DOPE, 33 mol% DOPC, 1 mol% LissRhod PE with 0.5% RAN Biotechnologies PEG-based fluorosurfactant diluted in FC-40. Relative quantitative mass spectrometry was performed using a Sciex QTRAP 4500 mass spectrometer hyphenated with a Shimadzu Nexera HPLC system. The instruments were controlled using Sciex Analyst 1.7 software. Samples were sonicated for 3 min and diluted 1 to 1000 in LCMS grade MeOH and subsequent fractionation was performed using a Supelco Titan C18 column (0.21 × 10 cm, 1.9 μ) operated at 45 °C. The isocratic method featured a flow rate of 0.5 mL/min using a 10 mM NH_4Ac solution in 98% MeOH aq. The MS experiments were performed in MRM mode using the following instrument settings: curtain gas 35 psi, ionization voltage 5500 V, nebulizer gas 30 psi, heater gas 60 psi, heater temperature 180 °C and a CAD gas set to 9. The following compound-specific parameters were used:

ID	Precursor mass [Da]	Fragment mass [Da]	Dwell time [msec]	Declustering potential [V]	Collision Energy [V]	Cell exit potential [V]
DOPE	744.498	603.500	110	91	33	16
DOTAP	662.528	603.500	50	166	41	20
DOPC	786.528	184.000	50	161	39	14
LissRhod	1301.605	682.000	110	40	67	24

MS experiments were performed in triplicates. Data analysis was performed using Sciex Analyst 1.7 and MultiQuant 3.0.2 software. Calculated concentrations were normalized using a SUV sample containing DOPE: DOTAP: DOPC: Liss Rhod PE with the following initial lipid ratios 33 : 33: 33 : 1.

4.6. Quantification of release efficiency and stability

Release efficiency and GUV mechanical stability after agitation were assessed by manually counting dsGUV and released GUVs with a Neubauer chamber mounted on a fluorescence microscope. The total lipid concentration of released and cleaned GUVs was quantified by measuring GUV solution fluorescence (Fig. S9). Respective fluorescence was normalized to a standard SUV dilution curve (fitted to one phase exponential decay) of known concentration and with equal ratios of fluorescently labeled lipids. For incubation of GUVs with cell lines total lipid concentrations between 1.5 μM and 50 μM were used.

4.7. Cell culture

REF52 cells, MDCK cells, A431 and A431D cells [50], Hela cells and Hs386 cells were cultured in Dulbecco's Modified Eagle Medium supplemented with 4.5 g/L glucose, 1% L-glutamine, 1% penicillin/streptomycin and 10% fetal bovine serum. SH-SY5Y cells were cultured in a 1:1 mixture of F12:DMEM supplemented with 1% L-glutamine, 1% penicillin/streptomycin and 10% fetal bovine serum. Jurkat cells were cultured in RPMI-1640 medium supplemented with 1% penicillin/streptomycin and 10% fetal bovine serum. PC12 were cultured in RPIM-1640 medium supplemented with 1% L-glutamine, 1% penicillin/streptomycin 5% fetal bovine serum and 10% heat-inactivated horse serum. Cell cultures were routinely cultured at 37 °C and 5% CO_2 atmosphere and passaged at ~80% confluency based on 0.05% trypsin/EDTA treatment. Jurkat cells were passaged by adding 1 mL of Jurkat culture to 4 mL of fresh culture medium.

4.8. Cell staining

Live cells were stained with Hoechst 33342 at a final concentration of 5 μg/mL to visualize cell nuclei. Cytoplasms were stained with CellTracker Blue CMAC dye and CellTracker Green CMFDA dye following the manufacturer's instructions. Lysosomes were stained with LysoTracker Green DND-26 dye following the manufacturer's instructions. Cell membranes were stained with wheat germ agglutinin (WGA)-AlexaFluor conjugates. Membranes were stained by adding WGA conjugates to a final concentration of 50 μg/mL to cells grown in fully supplemented growth medium for 10 min at room temperature. To reduce endocytotic dye uptake, stained cells were handled for imaging at room temperature. WGA was previously also used to stain for endosomal and Golgi-associated vesicles [51]. To stain endosomal GUV uptake, cells incubated with GUVs were incubated with a final concentration of 5 μg/mL WGA-AlexaFluor conjugates for 24 h.

4.9. Confocal microscopy and live cell imaging

For fluorescence confocal microscopy observations, cell lines were cultured in 8-well Nunc LabTeK glass bottom culture slides filled with minimum 400 μL of culture medium. Confocal microscopy was performed with a laser scanning microscope LSM 800 (Carl Zeiss AG). Images were acquired with a 20x (Objective Plan-Apochromat 20x/0.8 M27, Carl Zeiss AG) and a 63x immersion oil objective (Plan-Apochromat 63x/1.40 Oil DIC, Carl Zeiss AG). Images were analyzed with ImageJ (NIH). Adjustments of image brightness and contrast or background corrections were performed always on the whole image and special care was taken not to obscure or eliminate any information from the original image. For images with speckled noise signals, 2 pixel median filters were applied. For cell fixation prior to confocal microscopy analysis, cell cultures were washed twice with PBS and subsequently fixed with 2–4% PFA for a minimum of 20 min. For time-lapse live cell imaging a Leica DMi8 inverted fluorescent microscope equipped with a sCMOS camera and 10x HC PL Fluotar (NA 0.32, PH1) objective was used. Cells were cultured in 8-well Nunc LabTeK glass bottom culture slides in FluoroBrite DMEM (high glucose) medium supplemented with GlutaMAX, 10% FBS and 1% Pen/Strep.

4.10. Transmission electron microscopy

REF cells incubated for 16 h with GUVs were fixed in 2.5% glutaraldehyde dissolved in a 0.1 M Na_3PO_4 solution for 30 min at room temperature. Cells were further fixed in 0.4% uranyl acetate overnight. Fixed cells were subsequently dehydrated with a 50%, 60%, 70%, 80%, 90%, and 100% ethanol series and embedded in resin over night at 60 °C. 85 nm ultrathin sections were prepared and contrasted with lead acetate or osmium tetroxide. A Zeiss EM 10 CR transmission electron microscope was used for imaging. If necessary, image contrast, brightness and sharpness were adjusted using the built-in ImageJ plug-ins.

4.11. Flow cytometry

As Jurkat cells are a leukemia-derived cell line which grows in suspension, the attraction assay developed for adherent cells cannot be applied to them. To also evaluate the attraction of GUVs to such suspension cells, a flow cytometry-based assessment was performed. For flow cytometry analysis of the attraction between RGD-functionalized GUVs and Jurkat cells, Rhodamine B-GUVs with varying RGD density (see Table S1) were incubated with Jurkat cells for 24 h. Cells were subsequently centrifuged for 5 min at 250 g and the supernatant, which contained GUVs that were unbound or had not been taken up by cells, was discarded. Cells were resuspended in fresh culture medium and for each condition GUV fluorescence within the cells was quantified with a BD LSRFortessa Cell Analyzer (BD Bioscience) using the blue laser line in the PE channel ($\lambda_{em\ max} = 575$). A gate was then set to discriminate between Jurkat cells, debris and possible clumps based on the

acquisition of scattered parameters. Subsequently, singlet cells were extracted from the aforementioned Jurkat population. Lastly, based on this gating strategy, fluorescence intensity associated with the cells' periphery was recorded and quantified.

4.12. Attraction assay

Attraction assays were performed as outlined in Fig. S3. Cells were seeded in triplicates in 100 μL of their corresponding growth medium to form a confluent monolayer after 24 h of incubation in 96 flat-bottom well-plates. GUV (labeled with LissRhod PE lipids) solutions were added to a final lipid concentration of 1.5 μM and incubated for 24 h. Fluorescence in each well was measured using an Infinite M200 TECAN plate reader controlled by TECAN iControl software with an in-built gain optimization and excitation/emission setting adjusted to 550/585 nm. Subsequently, wells were washed 3x with 100 μL PBS using a multichannel pipette and residual fluorescence was measured again. Fluorescence intensity after washing was normalized to the intensity before washing in order to account for any variation in sample preparation. All samples were measured in triplicates at 4 individual positions per well in order to account for variations in cell monolayer density. For comparing the specific attraction of biofunctionalized GUVs to specific cell lines, all attraction values were normalized to the attraction of BSA functionalized GUVs and the respective cell line in order to reference all attraction values for each cell type to a common moderately non-reactive protein.

A total lipid concentration of 3 μM of anti-CD3 functionalized GUVs and Jurkat cells were incubated for 24 h in order to perform fluorescence confocal microscopy observations of the attraction and formation of contact sides. Prior to imaging, cells were stained with Hoechst 33342 and WGA-AlexaFluor 647 as described above.

4.13. Quantification of preferential GUV uptake in co-culture

To quantify preferential GUV uptake in SH-SY5Y/Hs683 co-culture experiments, SH-SY5Y and Hs683 cell were separately stained with CellTracker Blue CMAC and CellTracker Green CMFDA, respectively. Cells were co-seeded at a 10:1 SH-SY5Y:Hs683 ratio in a 1:1 mixture of F12:DMEM supplemented with 1% L-glutamine, 1% penicillin/streptomycin and 10% fetal bovine serum together with GUVs composed of 20 mol% PEG750 PE, 20 mol% EggPG, 58 mol% EggPC, 1 mol% LissRhod PE and 1 mol% palmitic acid-NHS coupled with 1.5 μM His-tagged recombinant NrCAM for 24 h. Cell cultures were subsequently washed 3x with PBS and fixed for 20 min with 4% PFA followed by fluorescence confocal microscopy analysis with appropriate laser excitation. The total area of SH-SY5Y and Hs683 cells in a field of view was calculated from single plane confocal images. The total number of GUVs in respective areas was determined by global threshold segmentation and subsequently normalized to the total cell area. *E.g.*, total area of SH-SY5Y and Hs683 cells (shown in Fig. 5c) is 20083.37 μm [2] and 40741.67 μm [2], respectively. They contain 1491 (= 0.0742 GUVs/μm [2]) and 578 (= 0.0141GUV/μm [2]) GUVs, respectively, which corresponds to an increase of 523% in the case of SH-SY5Y cells.

4.14. Encapsulation of baculoviruses

For intracellular delivery of baculoviruses (BVs), BVs were produced using the MultiBac baculovirus/insect cell system [52]. Solutions containing purified BVs were mixed in a 1:100 ratio with the SUV solution. Importantly, for dsGUV production, PBS with 60 mM $MgCl_2$ was used, as lower manganese concentrations inhibited dsGUV formation and release rates. Released and cleaned GUVs containing BVs were then incubated with REF cells for 24 h and subsequently stained with 8 μg/mL Hoechst33342. Expression of BV encoded mito-dsRed and BV localization was assessed my fluorescence confocal microscopy. For visualizing intracellular BV, staining of BV-DNA was imaged by overexposing the Hoechst33342 channel.

4.15. GUV biofunctionalization and PEGylation

GUV biofunctionalization was solely performed on released GUVs. If not stated otherwise, GUV functionalization was carried out in PBS buffer and in the dark on a horizontal shaker at room temperature. After functionalization, GUVs were centrifuged at > 10.000 g for a minimum of 15 min and resuspended in PBS. For NHS-based coupling reactions, GUVs were kept whenever possible at 4 °C and released from droplets not later than 1 h after production. NHS coupling reactions were performed over a minimum of 3 h. For NHS and NTA-based biofuntionalizations, respective proteins and peptide were added in 2–5 fold excess to total functionalized lipids as calculated from the total lipid concentration. For example, if fluorescence quantification showed a total lipid concentration of 150 μM (corresponding to an approx. Release efficiency of 10%) and GUVs were produced from SUVs with 1 mol% palmitic acid NHS lipids, then a minimum of 1.5 μM of the protein to be coupled was added (about 50% of the NHS-coupled lipids would reside within the inner membrane leaflet and not be accessible for coupling). In the case of the WGA coupling, lectin coupled to GUVs was employed at a 10 times lower molar concentration than the presented 5 mol% NHS ligand. GUV biofunctionalization with RGD peptides was performed by introducing a desired amount of DSPE-RGD into the lipid mixture for SUV production.

For the sequential functionalization of GUVs with gold nanoparticles (AuNP), GUVs containing 1 mol% NHS were incubated with 3 μM L-cysteine for 6 h. Subsequently, 50 nm Au nanoparticles were added to a final concentration of 10 μg/mL and the mixture was shaken at 300 rpm overnight. The functionalization of GUVs with IgG antibodies was performed by incubating 3 μM His-tag Protein G with GUVs containing 1 mol% 18:1 DGS-NTA(Ni) lipids for 1 h. Subsequently, a final concentration of 3 μM of respective IgG dissolved in 1% BSA was added to the mixture and incubated for 1 h. In order to avoid cross reactions whenever multiple functionalizations based on different coupling reactions were performed (as in the case of triple functionalization), proteins to be coupled *via* NHS were incubated with the GUVs first before performing other reactions like biotin-streptavidin coupling, for example.

PEGylation of GUVs with poly-ethylene-glycol polymers was performed by introducing a desired amount of PEG350 PE, PEG750 PE or PEG1000 PE into the lipid mixture for SUV production.

4.16. Lysosomal escape mechanisms

For all tested approaches, dsGUVs were produced in PBS with 10 mM $MgCl_2$ and 50 mM 8-Hydroxypyrene-1,3,6-trisulfonic acid trisodium salt using 1.25 mM triblock PFPE-PEG-PFPE 2500-600-2500 surfactant dissolved in FC-40. Released GUVs were cleaned by centrifugation and incubated with REF cells for 24 h. Intracellular HPTS fluorescence distribution was subsequently assessed by fluorescence confocal microscopy. Imaging parameters were kept constant when comparing the different approaches.

Poly-ethylene-imine (PEI): For lysosomal escape analysis using the PEI proton sponge mechanism, GUVs composed of 20 mol% EggPG, 79 mol% EggPC and 1 mol% LissRhod PE were loaded with 44 μg/mL poly-ethylene-imine during droplet production.

GALA peptide: For lysosomal escape analysis using GALA-mediated intralysosomal fusion, GUVs composed of 1 mol% LissRhod PE, 1 mol% palmitic acid NHS, 20 mol% EggPG and 79 mol% EggPC were released and then coupled with 1.5 μM GALA peptide (EAALAE ALAEALAEHLAEALAEALEALA) in PBS.

DOBAQ: For lysosomal escape analysis using DOBAQ-mediated intralysosomal fusion, GUVs composed of 1 mol% LissRhod PE, 60 mol% DOBAQ, 20 mol% EggPG and 19 mol% EggPC were produced with PBS containing additional 50 mM HEPES for pH stabilization.

Data availability

The raw data required to reproduce these findings are available upon request to the corresponding authors. The processed data required

to reproduce these findings are available upon request to the corresponding authors.

Credit author statement

Oskar Staufer: Conceptualization, Methodology, Writing - original draft, performed most of the experimental work, Formal analysis, The final version of the manuscript was approved. **Silvia Antona:** Formal analysis, planed flow cytometry experiments, The final version of the manuscript was approved. **Dennis Zhang:** Formal analysis, The final version of the manuscript was approved. **Júlia Csatári:** performed primary hippocampal neuron experiments, The final version of the manuscript was approved. **Martin Schröter:** synthesized block-copolymer surfactants, The final version of the manuscript was approved. **Jan-Willi Janiesch:** synthesized block-copolymer surfactants, The final version of the manuscript was approved. **Sebastian Fabritz:** Formal analysis, The final version of the manuscript was approved. **Imre Berger:** provided baculoviruses, Conceptualization, The final version of the manuscript was approved. **Ilia Platzman:** Conceptualization, Methodology, Writing - original draft, Supervision, The final version of the manuscript was approved. **Joachim P. Spatz:** Conceptualization, Methodology, Writing - original draft, Supervision, The final version of the manuscript was approved.

Declaration of competing interest

The authors declare that they have no known competing financial interests or personal relationships that could have appeared to influence the work reported in this paper.

Acknowledgments

The authors acknowledge funding from the Federal Ministry of Education and Research of Germany, Grant Agreement no. 13XP5073A, PolyAntiBak and the MaxSynBio Consortium, the later is jointly funded by the Federal Ministry of Education and Research of Germany and the Max Planck Society. They also acknowledge the support from the Volkswagen Stiftung (priority call 'Life?') and the BBSRC/EPSRC Research Centre for synthetic biology at the University of Bristol BrisSynBio (BB/L01386X/1). The authors are grateful to Andrea Hellwig (Interdisciplinary Centre for Neurosciences Heidelberg) for technical assistance during TEM preparation and imaging as well as Martin Pelosse and Julia Ricken for production and purification of baculoviruses and recombinant GFP, respectively. The authors thank the laboratory of Hilmar Bading, Department of Neurobiology and IZN, Heidelberg University, for providing primary hippocampal neurons. The authors further thank the MS Core Facility (MPI for Medical Research) for technical assistance and performance of mass spectrometry analysis. O.S. acknowledges support from the Heidelberg Biosciences International Graduate School and the Max Planck School Matter to Life. O.S. is the Meurer Visiting Professor at the Max Planck Center for Minimal Biology, Bristol. I.B. is investigator of the European Research Council (ERC-2018-ADG 834631 DNA-DOCK). J.P.S. is the Weston Visiting Professor at the Weizmann Institute of Science and part of the excellence cluster CellNetworks at the University of Heidelberg. The Max Planck Society is appreciated for its general support.

Appendix A. Supplementary data

Supplementary data to this article can be found online at https://doi.org/10.1016/j.biomaterials.2020.120203.

References

[1] Q. Chaudhry, et al., Applications and implications of nanotechnologies for the food sector, Food Addit. Contam. Part A, Chemistry, analysis, control, exposure & risk assessment 25 (2008) 241–258, https://doi.org/10.1080/02652030701744538.
[2] Y. Rahimpour, H. Hamishehkar, Liposomes in cosmeceutics, Expet Opin. Drug Deliv. 9 (2012) 443–455, https://doi.org/10.1517/17425247.2012.666968.
[3] A.V. Kristen, et al., Patisiran, an RNAi therapeutic for the treatment of hereditary transthyretin-mediated amyloidosis, Neurodegener. Dis. Manag. 9 (2019) 5–23, https://doi.org/10.2217/nmt-2018-0033.
[4] I.A. Bakker-Woudenberg, M.T. ten Kate, L. Guo, P. Working, J.W. Mouton, Ciprofloxacin in polyethylene glycol-coated liposomes: efficacy in rat models of acute or chronic Pseudomonas aeruginosa infection, Antimicrob. Agents Chemother. 46 (2002) 2575–2581.
[5] Z. Drulis-Kawa, A. Dorotkiewicz-Jach, Liposomes as delivery systems for antibiotics, Int. J. Pharm. 387 (2010) 187–198, https://doi.org/10.1016/j.ijpharm.2009.11.033.
[6] T.M. Allen, Liposomal drug formulations. Rationale for development and what we can expect for the future, Drugs 56 (1998) 747–756, https://doi.org/10.2165/00003495-199856050-00001.
[7] A. Sharma, U.S. Sharma, Liposomes in drug delivery: progress and limitations, Int. J. Pharm. 154 (1997) 123–140, https://doi.org/10.1016/S0378-5173(97)00135-X.
[8] T. Nii, F. Ishii, Encapsulation efficiency of water-soluble and insoluble drugs in liposomes prepared by the microencapsulation vesicle method, Int. J. Pharm. 298 (2005) 198–205, https://doi.org/10.1016/j.ijpharm.2005.04.029.
[9] J. Gubernator, Active methods of drug loading into liposomes: recent strategies for stable drug entrapment and increased in vivo activity, Expet Opin. Drug Deliv. 8 (2011) 565–580, https://doi.org/10.1517/17425247.2011.566552.
[10] M. Ryvolova, et al., Modern micro and nanoparticle-based imaging techniques, Sensors 12 (2012) 14792–14820, https://doi.org/10.3390/s121114792.
[11] A. Udomprasert, T. Kangsamaksin, DNA origami applications in cancer therapy, Canc. Sci. 108 (2017) 1535–1543, https://doi.org/10.1111/cas.13290.
[12] J.C. Stachowiak, et al., Unilamellar vesicle formation and encapsulation by microfluidic jetting, Proc. Natl. Acad. Sci. U. S. A 105 (2008) 4697–4702, https://doi.org/10.1073/pnas.0710875105.
[13] A.C. Saito, T. Ogura, K. Fujiwara, S. Murata, S.M. Nomura, Introducing micrometer-sized artificial objects into live cells: a method for cell-giant unilamellar vesicle electrofusion, PloS One 9 (2014) e106853, , https://doi.org/10.1371/journal.pone.0106853.
[14] J. Griesemer, The enduring value of Gánti's chemoton model and life criteria: heuristic pursuit of exact theoretical biology, J. Theor. Biol. 381 (2015) 23–28, https://doi.org/10.1016/j.jtbi.2015.05.016.
[15] L.R. Arriaga, et al., Ultrathin shell double emulsion templated giant unilamellar lipid vesicles with controlled microdomain formation, Small 10 (2014) 950–956, https://doi.org/10.1002/smll.201301904.
[16] S. Deshpande, Y. Caspi, A.E.C. Meijering, C. Dekker, Octanol-assisted liposome assembly on chip, Nat. Commun. 7 (2016) 10447, https://doi.org/10.1038/ncomms10447.
[17] Y. Elani, et al., Constructing vesicle-based artificial cells with embedded living cells as organelle-like modules, Sci. Rep. 8 (2018) 4564, https://doi.org/10.1038/s41598-018-22263-3.
[18] D.J. Paterson, J. Reboud, R. Wilson, M. Tassieri, J.M. Cooper, Integrating microfluidic generation, handling and analysis of biomimetic giant unilamellar vesicles, Lab Chip 14 (2014) 1806–1810, https://doi.org/10.1039/C4LC00199K.
[19] K. Gopfrich, I. Platzman, J.P. Spatz, Mastering complexity: towards bottom-up construction of multifunctional eukaryotic synthetic cells, Trends Biotechnol. 36 (2018) 938–951, https://doi.org/10.1016/j.tibtech.2018.03.008.
[20] E. Jenkins, et al., Reconstitution of immune cell interactions in free-standing membranes, J. Cell Sci. 132 (2018), https://doi.org/10.1242/jcs.219709.
[21] T. Noyhouzer, et al., Ferrocene-modified phospholipid: an innovative precursor for redox-triggered drug delivery vesicles selective to cancer cells, Langmuir 32 (2016) 4169–4178, https://doi.org/10.1021/acs.langmuir.6b00511.
[22] M. Weiss, et al., Sequential bottom-up assembly of mechanically stabilized synthetic cells by microfluidics, Nat. Mater. (2017), https://doi.org/10.1038/nmat5005.
[23] B. Haller, et al., Charge-controlled microfluidic formation of lipid-based single- and multicompartment systems, Lab Chip 18 (2018) 2665–2674, https://doi.org/10.1039/c8lc00582f.
[24] K. Göpfrich, et al., One-pot assembly of complex giant unilamellar vesicle-based synthetic cells, ACS Synth. Biol. (2019), https://doi.org/10.1021/acssynbio.9b00034.
[25] L. Shui, A. van den Berg, J.C.T. Eijkel, Scalable attoliter monodisperse droplet formation using multiphase nano-microfluidics, Microfluid. Nanofluidics 11 (2011) 87–92, https://doi.org/10.1007/s10404-011-0776-7.
[26] J.-u. Shim, et al., Ultrarapid generation of femtoliter microfluidic droplets for single-molecule-counting immunoassays, ACS Nano 7 (2013) 5955–5964, https://doi.org/10.1021/nn401661d.
[27] A.C. Hatch, et al., 1-Million droplet array with wide-field fluorescence imaging for digital PCR, Lab Chip 11 (2011) 3838–3845, https://doi.org/10.1039/C1LC20561G.
[28] B. Verbruggen, et al., Design of a flow-controlled asymmetric droplet splitter using computational fluid dynamics, Microfluid. Nanofluidics 15 (2013) 243–252, https://doi.org/10.1007/s10404-013-1139-3.
[29] A.A. Gabizon, Liposome circulation time and tumor targeting: implications for cancer chemotherapy, Adv. Drug Deliv. Rev. 16 (1995) 285–294, https://doi.org/10.1016/0169-409X(95)00030-B.
[30] S. Sofou, G. Sgouros, Antibody-targeted liposomes in cancer therapy and imaging, Expet Opin. Drug Deliv. 5 (2008) 189–204, https://doi.org/10.1517/17425247.5.2.189.
[31] F. Wang, L. Chen, R. Zhang, Z. Chen, L. Zhu, RGD peptide conjugated liposomal drug delivery system for enhance therapeutic efficacy in treating bone metastasis from prostate cancer, J. Contr. Release 196 (2014) 222–233, https://doi.org/10.1016/j.jconrel.2014.10.012.

[32] R. De Marco, et al., Selective detection of alpha4beta1 integrin (VLA-4)-expressing cells using peptide-functionalized nanostructured materials mimicking endothelial surfaces adjacent to inflammatory sites, Biopolymers (2017), https://doi.org/10.1002/bip.23081.
[33] M.L. Immordino, F. Dosio, L. Cattel, Stealth liposomes: review of the basic science, rationale, and clinical applications, existing and potential, Int. J. Nanomed. 1 (2006) 297–315.
[34] M. Sangrà, J. Estelrich, R. Sabaté, A. Espargaró, M.A. Busquets, Evidence of protein adsorption in pegylated liposomes: influence of liposomal decoration, Nanomaterials 7 (2017) 37, https://doi.org/10.3390/nano7020037.
[35] E.T. Stoeckli, L.T. Landmesser, Axonin-1, Nr-CAM, and Ng-CAM play different roles in the in vivo guidance of chick commissural neurons, Neuron 14 (1995) 1165–1179.
[36] B. Rathore, et al., Nanomaterial designing strategies related to cell lysosome and their biomedical applications: a review, Biomaterials 211 (2019) 25–47, https://doi.org/10.1016/j.biomaterials.2019.05.002.
[37] A. Sharma, K. Vaghasiya, E. Ray, R.K. Verma, Lysosomal targeting strategies for design and delivery of bioactive for therapeutic interventions, J. Drug Target. 26 (2018) 208–221, https://doi.org/10.1080/1061186x.2017.1374390.
[38] T. Bus, A. Traeger, U.S. Schubert, The great escape: how cationic polyplexes overcome the endosomal barrier, J. Mater. Chem. B 6 (2018) 6904–6918, https://doi.org/10.1039/C8TB00967H.
[39] I. Nakase, K. Kogure, H. Harashima, S. Futaki, Application of a fusiogenic peptide GALA for intracellular delivery, Methods Mol. Biol. 683 (2011) 525–533, https://doi.org/10.1007/978-1-60761-919-2_37.
[40] S. Draffehn, M.U. Kumke, Monitoring the collapse of pH-sensitive liposomal nanocarriers and environmental pH simultaneously: a fluorescence-based approach, Mol. Pharm. 13 (2016) 1608–1617, https://doi.org/10.1021/acs.molpharmaceut.6b00064.
[41] S.R. Elkin, et al., A systematic analysis reveals heterogeneous changes in the endocytic activities of cancer cells, Canc. Res. 75 (2015) 4640–4650, https://doi.org/10.1158/0008-5472.can-15-0939.
[42] E. Knecht, J. Hernandez-Yago, S. Grisolia, Regulation of lysosomal autophagy in transformed and non-transformed mouse fibroblasts under several growth conditions, Exp. Cell Res. 154 (1984) 224–232.
[43] S.J. Zhang, et al., Decoding NMDA receptor signaling: identification of genomic programs specifying neuronal survival and death, Neuron 53 (2007) 549–562, https://doi.org/10.1016/j.neuron.2007.01.025.
[44] M. Mansouri, et al., Highly efficient baculovirus-mediated multigene delivery in primary cells, Nat. Commun. 7 (2016) 11529, https://doi.org/10.1038/ncomms11529.
[45] C. Hofmann, et al., Efficient gene transfer into human hepatocytes by baculovirus vectors, Proc. Natl. Acad. Sci. U. S. A 92 (1995) 10099–10103, https://doi.org/10.1073/pnas.92.22.10099.
[46] K. Gupta, et al., MultiBac: baculovirus-mediated multigene DNA cargo delivery in insect and mammalian cells, Viruses 11 (2019), https://doi.org/10.3390/v11030198.
[47] D. Missirlis, et al., Substrate engagement of integrins alpha5beta1 and alphavbeta3 is necessary, but not sufficient, for high directional persistence in migration on fibronectin, Sci. Rep. 6 (2016) 23258, https://doi.org/10.1038/srep23258.
[48] Y.X. and, G.M. Whitesides, Soft lithography, Annu. Rev. Mater. Sci. 28 (1998) 153–184, https://doi.org/10.1146/annurev.matsci.28.1.153.
[49] M.C. Howland, A.W. Szmodis, B. Sanii, A.N. Parikh, Characterization of physical properties of supported phospholipid membranes using imaging ellipsometry at optical wavelengths, Biophys. J. 92 (2007) 1306–1317, https://doi.org/10.1529/biophysj.106.097071.
[50] J.E. Lewis, et al., Cross-talk between adherens junctions and desmosomes depends on plakoglobin, J. Cell Biol. 136 (1997) 919–934.
[51] T. Kanazawa, H. Takematsu, A. Yamamoto, H. Yamamoto, Y. Kozutsumi, Wheat germ agglutinin stains dispersed post-golgi vesicles after treatment with the cytokinesis inhibitor psychosine, J. Cell. Physiol. 215 (2008) 517–525, https://doi.org/10.1002/jcp.21328.
[52] D. Sari, et al., The MultiBac baculovirus/insect cell expression vector system for producing complex protein biologics, Adv. Exp. Med. Biol. 896 (2016) 199–215, https://doi.org/10.1007/978-3-319-27216-0_13.
[54] Oskar Staufer, Martin Schröter, Ilia Platzman, Joachim Spatz, Bottom-up assembly of functional intracellular synthetic organelles by droplet-based microfluidics, Small 16 (27) (2020), https://doi.org/10.1002/smll.201906424.